



HAL
open science

Experimental investigation on the effect of load distribution on the performances of a counter-rotating axial-flow fan

Florent Ravelet, F. Bakir, C. Sarraf, J. Wang

► **To cite this version:**

Florent Ravelet, F. Bakir, C. Sarraf, J. Wang. Experimental investigation on the effect of load distribution on the performances of a counter-rotating axial-flow fan. *Experimental Thermal and Fluid Science*, 2018, 96, pp.101. 10.1016/j.expthermflusci.2018.03.004 . hal-01610997v2

HAL Id: hal-01610997

<https://hal.science/hal-01610997v2>

Submitted on 5 Feb 2018

HAL is a multi-disciplinary open access archive for the deposit and dissemination of scientific research documents, whether they are published or not. The documents may come from teaching and research institutions in France or abroad, or from public or private research centers.

L'archive ouverte pluridisciplinaire **HAL**, est destinée au dépôt et à la diffusion de documents scientifiques de niveau recherche, publiés ou non, émanant des établissements d'enseignement et de recherche français ou étrangers, des laboratoires publics ou privés.

Experimental investigation on the effect of load distribution on the performances of a counter-rotating axial-flow fan

F. Ravelet^{a,*}, F. Bakir^a, C. Sarraf^a, J. Wang^a

^a*DynFluid, Arts et Métiers-ParisTech, 151 Bld de l'Hôpital, 75013 Paris, France*

Abstract

In the design procedure of a counter-rotating axial-flow stage, parameters such as the angular velocity ratio and the repartition of the work performed by each rotors are to be chosen. In the present Article, three counter-rotating stages are designed to meet the same working point. These stages have different repartitions of load between the front and rear rotor, different angular velocity ratios or mean stagger angles of the blades of the front rotors. The stage global characteristics and the unsteady features of the flow between the counter-rotating rotors are measured and compared. The three systems all have satisfying overall performances at the design point. Strong differences are observed in the flow field at partial flow rates, the rear rotor reducing the hub recirculation. The behaviour at partial flow rates is thus triggered by the rear rotor characteristics. The best compromise is obtained with a repartition of the loading of 60% for the front rotor and 40% for the rear rotor, with almost equal angular velocities.

Keywords: Counter-rotating axial-flow fan, turbomachinery, global performance, pressure fluctuations.

1. Introduction

Counter-rotating axial turbomachines such as propellers, axial-flow pumps and low-speed fans are used in various industrial domains [1–7]. In a counter-rotating stage (CRS), the front rotor (FR) and the rear rotor (RR) rotate in opposite directions (see Fig. 1). The rear rotor has two functions: it converts part of the rotational kinetic energy of the flow coming from the front rotor to static head and also supplies energy to the fluid. A high performance and compact turbomachine can therefore been designed, with a reduction of the rotational speed and a better homogenization of the flow downstream of the stage, compared to a single rotor or rotor-stator stage [8–10]. On the other hand, counter-rotating turbomachines present some drawbacks such as an increase in mechanical complexity, or a potential increase in noise generation.

One of the difficulties in the design of such machines is the presence of highly unsteady flows in the mixing area between the rotors. Strong unsteady interactions between the rotors may lead to large acoustic noise emission [11] and may affect the performances of the stage [12, 13]. When designing a counter-rotating stage, some parameters such as the distribution of the total work between the two rotors or the ratio of the rotation rates have to be chosen, this choice being most often somehow arbitrary. Few studies have been carried out about the effects of design parameters on the stage performances and on its unsteady flow features.

For instance, Shigemitsu *et al.* [1] compare two counter-rotating pumps with the same front rotor and two different rear rotors. They conclude that the pressure field of the front rotor is strongly influenced by the rear rotor. The unsteady pressure fluctuations are dominated by the rear rotor blade passing frequency, and are located close to the front rotor. In subsequent works [2, 8], they also compare a counter-rotating pump with a rotor-stator stage and perform Laser Doppler Velocimetry measurement, focusing on the rotor-rotor interaction at partial flow rate. They propose that decreasing the rear rotor rotational speed and stagger angle would be beneficial for the stable operation of the pump, by suppressing the back flow region at the inlet tip region of the rear rotor. They eventually observe that the blockage effect of the rear rotor on the flow field close to the front rotor blades trailing edges seems stronger than the effects of the front rotor wake on the rear rotor.

The effect of the axial distance between the counter-rotating rotors of an axial-flow fan is studied by Shigemitsu *et al.* [5]. They conclude that the influence of this distance on static pressure rise is stronger at partial flow rate than at design flow rate. The axial distance exhibits a slight influence on the static pressure rise of the front rotor, the static pressure of the rear rotor decreasing gradually as the distance increases above 1.25 mean chord length of the front rotor blades.

Among the few studies dedicated to the design procedure of a counter-rotating stage one can cite the works of Cho *et al.* [14] who use a conventional design method based on the simplified meridional flow method with the radial equilibrium equation and the free vortex design con-

*corresponding author

Email address: florent.ravelet@ensta.org (F. Ravelet)

dition, and study the effect of parameters such as the hub to tip ratio, or the solidity. Cao *et al.* [15] used Computational Fluid Dynamics results to re-design the rear rotor of a counter-rotating pump and obtain an increase in performances with respect to the original rear rotor conventional design. Finally, in the Dynfluid Laboratory from Arts et Métiers-ParisTech University, series of experiments focused on the validation of an original design method for ducted low-speed counter-rotating axial-flow fans have been performed [9]. Based on this work, three different counter-rotating stages (JW1, JW2 and JW3) have been designed to attain the same specifications, while varying the distribution of the work performed by the front and rear rotors. First results on the global performances of the three stages close to the nominal flow rate have been presented in Ref. [16], for different axial distances between the front and rear rotors and for various rotation rates of the rear rotors.

In the present Article, the study of these three counter-rotating stages is firstly extended to very partial flow rates, and is supplemented with an analysis of local velocity profiles. The three stages are studied at a fixed axial distance between the front and rear rotors and at their nominal angular velocity ratios. The peculiar specifications of each of the three stages are briefly recalled in § 2. Then, the experimental setup and an analysis of the uncertainty of the measurements are reported in § 3. The features of the three stages are analyzed and compared in § 4: the overall performances are discussed in § 4.1, then the time-averaged velocity profiles in between the front and rear rotors are studied in § 4.2, and finally unsteady features are explored in § 4.3. Concluding remarks are then given in § 5.

2. Design and geometry of the three counter-rotating stages

2.1. Specifications and design procedure

In the design procedure of a CRS that has been developed at the DynFluid Laboratory [9], the front rotor is first designed to achieve a part of the total pressure rise at the design flow rate. This is done with the in-house software MFT (Mixed Flow Turbomachinery), described in Ref. [17]. Please note that the *total* pressure rise that is considered is the difference of total pressure between the inlet and the outlet of a rotor and thus includes the contribution of the tangential kinetic energy. In the present case, the front rotors of the three systems are designed with the same radial distribution of the blade loading. It consists of a “Constant Vortex” Design [18, 19], *i.e.* the Euler work per unit mass increases linearly from the hub to the tip of the blades or equivalently the blade loading that is the ratio of the Euler work to the square of the peripheral velocity is decreasing like $1/r$ along the radial direction. From the specified total pressure rise, hub and tip radii (R_{tip} and R_{hub}), volume flow-rate and rotating speed, the velocity

triangles are computed for 11 radial sections, based on the Euler equation for perfect fluid with a rough estimate of the efficiency of $\eta_{est} = 60\%$ and on the equation of simplified radial equilibrium (radial momentum conservation). The blades are then defined by the local resolution of an inverse problem, searching for the best suited cascade to the proposed velocity triangles. The blade cascade is defined by a NACA65-series blade of aerodynamic camber $C_{z\infty 0}$ and stagger angle γ and by the cascade solidity σ . The MFT software is based on empirical correlations of the characteristics of NACA65-series blade cascades that have been fitted on the results published in Ref. [20]—these correlations having been validated for $0.5 \leq \sigma \leq 1.5$ and $0 \leq C_{z\infty 0} \leq 2.7$ [17].

Then, a simple 1D analysis—including semi-empirical loss models fitted on the results published in Ref. [20] and the introduction of the effect of the hub and casing boundary layers with velocity deficit laws—is used to predict the axial and tangential velocity profiles at the outlet of the front rotor. All the details are available in Ref. [17]. These profiles are taken as the inlet conditions for the conception of the rear rotor that is designed with two constraints: the angular velocity is set to meet the required total pressure rise, and the profiles of camber, solidity and stagger angles of the blade cascade are chosen such that the absolute tangential velocity at the outlet of the stage vanishes (pure axial velocity profile). The rear rotors are thus designed to realign the outflow of the front rotors toward the axial direction which leads to not usual shapes blade loading profiles of the rear rotors, with non-monotonic stagger angle and blade camber profiles (see Fig. 3 in Ref. [16] and Tab. 3 in the present Article).

D (mm)	R_{hub} (mm)	R_{tip} (mm)	Δp_t (Pa)	Δp_s (Pa)	Q_v ($\text{m}^3 \cdot \text{s}^{-1}$)
380	65	187.5	420	373	1

Table 1: Common specifications of the three CRS: geometrical constraints and design point. D stands for the diameter of the pipe, R_{hub} and R_{tip} for the radii of the rotors at hub and tip, Δp_t for the *total* pressure rise, Δp_s for the *static* pressure rise according to the ISO-5801 standard and Q_v for the volumetric flow rate. The values correspond to air with a density $\rho_a = 1.21 \text{ kg} \cdot \text{m}^{-3}$

The common specifications of the three stages—JW1, JW2 and JW3—are presented in Tab. 1. The volumetric flow rate and total pressure rise are the same as for the first prototype—HSN—described and analyzed in Ref. [9]. All the rotors are made of blades of circular-arc camber lines, with NACA65 profiles. The hub-to-tip radius ratio is constant and equal to $R_{hub}/R_{tip} = 0.347$. It has been increased with respect to the HSN prototype in order to have the same radius for the fan hub and for the driving motor casings. The radial gap between the rotor tip and casing is 2.5 mm, that is 2% of the blade span. All the rotors have the same inner and outer radii.

	L %	$N_{FR} N_{RR}$ (rpm)	θ_0	$Z_{FR} Z_{RR}$
JW1	41	2300 2200	0.96	10 7
JW2	52	1800 2600	1.44	13 7
JW3	23	2600 1100	0.42	10 7

Table 2: Design parameters of the three CRS. The rotation rates of the front rotor and rear rotors are respectively N_{FR} and N_{RR} . The nominal angular velocity ratio is $\theta_0 = N_{RR}/N_{FR}$. The parameter L is the load distribution ratio at design point (see text). The number of blades of the Front Rotor and rear rotors are respectively Z_{FR} and Z_{RR}

2.2. Geometry of the three different CRS

The parameters that are used to design the 3 counter-rotating stages are presented in Tab. 2, and the resulting geometries of the blade cascades of the rotors are described in Tab. 3. The load distribution ratio L is defined as the ratio of the total pressure rise due to the rear rotor to that of the counter-rotating stage at the design flow rate:

$$L = \frac{\Delta p_{t, RR}}{\Delta p_t} \quad (1)$$

The peculiar features of each CRS are the following:

JW1. This CRS is very similar to the configuration HSN that was studied in Refs. [9, 10], with very similar parameters (load distribution ratio $L \simeq 40\%$, rotation rates and angular velocity ratio $\theta \simeq 1$). One difference is that the front rotor of JW1 ($JW1_{FR}$) has larger stagger angles with respect to that of HSN.

JW2. This one corresponds to the highest load distribution ratio ($L = 52\%$) that was compatible with the geometrical and technical constraints of our experiments (*e.g.* maximum rotation rate of the motors). In this counter-rotating stage, the rear rotor transfers a little bit more energy to the fluid than the front rotor does, and thus $JW2_{FR}$ possesses the lowest pressure rise among the three front rotors. It is furthermore designed with low stagger angles. The rear rotor rotates 1.44 times faster than the front rotor in that configuration. The Reynolds number based on the blade chord length and on the relative velocity is fairly low for the front rotor, which may lead to a reduced efficiency [21].

JW3. This stage correspond to the opposite case, with the lowest $L = 23\%$ and a rear rotor that rotates much more slowly than the front rotor, $JW3_{FR}$, which may have the highest and steepest characteristics among the front rotors working alone.

3. Experimental setup

The test rig is built according to the ISO-5801 standard and has been described in Refs. [9, 16]. A sketch of the experimental setup is shown in Fig. 1. The test bench consists of a cylindrical pipe of inner diameter $D = 380$ mm.

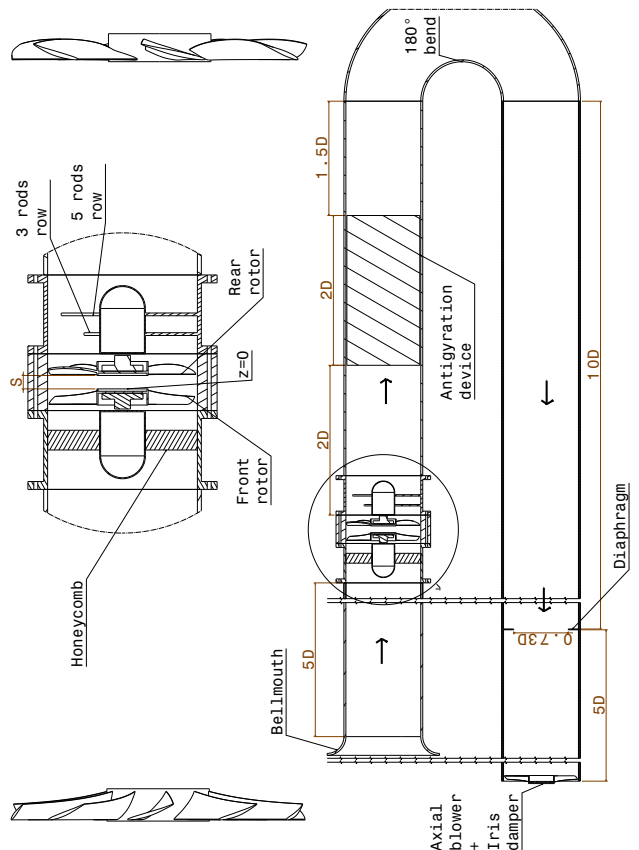


Figure 1: Sketch of the experimental set-up, with a detailed view of the counter-rotating stage. The axial distances are measured from the aft of the hub of the front rotor

		R (mm)	γ ($^\circ$)	L_{chord} (mm)	σ	\mathcal{D}	Profile	Re
FR of JW1	hub	65	40.7	47.2	1.2	0.55	NACA65(15)11	5.9×10^4
	midspan	126.5	63.5	54.6	0.7		NACA65(08)09	1.2×10^5
	tip	187.5	71.6	62.0	0.5	0.37	NACA65(06)08	1.9×10^5
FR of JW2	hub	65	27.6	42.5	1.4	0.57	NACA65(21)12	4.5×10^4
	midspan	126.5	55.2	44.3	0.7		NACA65(14)11	7.7×10^4
	tip	187.5	66.4	46.1	0.5	0.52	NACA65(10)11	1.1×10^5
FR of JW3	hub	65	42.9	43.0	1.1	0.62	NACA65(17)12	5.8×10^4
	midspan	126.5	65.5	51.1	0.6		NACA65(09)10	1.2×10^5
	tip	187.5	73.1	59.2	0.5	0.39	NACA65(07)08	2.1×10^5
RR of JW1	hub	65	75.3	49.2	0.8	0.68	NACA65(04)12	9.3×10^4
	midspan	126.5	68.1	67.3	0.6		NACA65(04)09	1.7×10^5
	tip	187.5	76.9	85.4	0.5	0.37	NACA65(03)07	3.0×10^5
RR of JW2	hub	65	74.9	48.6	0.8	0.52	NACA65(03)12	9.5×10^4
	midspan	126.5	70.8	67.1	0.6		NACA65(03)09	1.9×10^5
	tip	187.5	78.3	85.6	0.5	0.31	NACA65(02)07	3.5×10^5
RR of JW3	hub	65	66.9	53.6	0.9	0.44	NACA65(04)11	8.3×10^4
	midspan	126.5	55.3	70.1	0.6		NACA65(10)09	1.1×10^5
	tip	187.5	68.6	86.6	0.5	0.63	NACA65(07)07	1.9×10^5

Table 3: Blade cascade parameters of the rotors. R is the radius, γ the stagger angle, L_{chord} the chord length, σ the solidity and \mathcal{D} the Lieblein's diffusion factor. The blade profile is a NACA65(xx)yy with xx standing for the relative camber and yy representing the relative thickness. The Reynolds number Re is based on the relative velocity and chord length at each radius at the design flow rate $Q_v = 1\text{m}^3.\text{s}^{-1}$, for air with a density $\rho_a = 1.21\text{ kg.m}^{-3}$ and a dynamic viscosity $\mu = 1.8 \times 10^{-5}\text{ Pa.s}$

Two brushless PANASONIC A4 motors drive each rotor separately and are hidden in a casing of diameter $0.32D$ and of length $0.45D$, with a warhead-shape end. The front and the rear motors are bound to the tube by two rod rows (3 and 5 rods, the first row being at $0.1D$ from the rotors). Please note that the flow is homogenized by a honeycomb situated upstream of the front rotor, the rod rows being hidden into the honeycomb. An anti gyration device is placed $2D$ downstream of the stage to remove the rotational component of the flow and to homogenize the flow before the measurements of the static pressure. It is made of eight metal sheets of thickness 1.5 mm and length $2D$, according to the ISO-5801 standard. The static pressure is measured $1D$ downstream of the anti gyration device through four flush-mounted pressure taps. A half-turn bend is then used to reduce the axial overcrowding. The volumetric flow rate is measured with an ISO-5167 standard diaphragm, located $10D$ downstream of the tube bend and $5D$ upstream of the pipe outlet. The diaphragm has a diameter $d = 0.73D$. Finally, the flow is regulated by an axial blower and an iris damper before being discharged into the ambient atmosphere. In the present Article, the distance between the rotors is fixed to 10 mm, which corresponds to 8.2% of the blade span, or approximately 20% of the average chord length of the front rotors and 15% of the average chord length of the rear rotors.

3.1. Measured and derived quantities

Measured quantities and accuracy. The atmospheric pressure p_a is measured with an accuracy of 100 Pa.

The dry temperature T_{ad} and the wet temperature T_{aw} are measured with a Fluke 51 Series II thermometer with an accuracy of $0.05\% + 0.3\text{ K}$.

The static pressure rise without correction Δp_v is the pressure difference between the four pressure taps down-

stream of the anti-gyration device and the atmosphere. It is measured with a Furness Control differential pressure transmitter FCO318, scaled at $\pm 2.5\text{ kPa}$, with an accuracy of 0.25% of reading.

The volumetric flow rate is measured with an ISO-5167 orifice plate. The pressure drop through the orifice plate Δp_q is measured with the same differential pressure transmitter.

In order to eliminate the pressure drop caused by the experimental facilities such as the honeycomb, the driving motor housing and the anti-gyration device, the static pressure drop has been measured without rotors, using the axial blower at the outlet of the test rig to create the flow. Then this pressure drop Δp_{drop} is modelled as a function of the orifice plate pressure drop Δp_q .

The torques applied to the rotors τ are measured by the Panasonic Minas A4 servo-controllers of the brushless AC motors. The value given by the servo-controllers has been calibrated against a HBM TW20N rotating torquemeter of accuracy 0.02 N.m. The agreement between the two values is within 0.1%. The measured value is corrected by the torque measured when the rotors are removed from the shaft.

The angular velocity of the two rotors ω is regulated within $\pm 2\text{ rpm}$.

Derived quantities. The actual density of air ρ_a is evaluated according to the ISO-5801 standard, by measuring the atmospheric pressure p_a , the dry temperature T_{ad} and the wet temperature T_{aw} , from which the partial pressure of the water vapour p_{wv} is computed:

$$\rho_a = \frac{p_a - 0.378p_{wv}}{287T_{ad}} \quad (2)$$

The volumetric flow rate is deduced from the measure-

ment of the pressure drop through the orifice plate Δp_q according to the ISO-5167 standard:

$$Q_v = \frac{\alpha \epsilon \pi d^2}{4} \sqrt{2 \frac{\Delta p_q}{\rho_a}} \quad (3)$$

In this equation, the coefficient ϵ takes into account the effects of compressibility and is here $0.998 \leq \epsilon \leq 1$. The coefficient α depends on the ratio of the diaphragm diameter to the pipe diameter, and depends slightly on the Reynolds number. In the range that is explored here, $0.726 \leq \alpha \leq 0.732$.

The static pressure rise of the CRS Δp_s is the difference between the static pressure downstream of the CRS and the inlet total pressure and is a combination of different measured quantities:

$$\Delta p_s = \Delta p_v + \Delta p_{drop} - \frac{1}{2} \rho_a \left(\frac{Q_v}{\pi D^2 / 4} \right)^2 \quad (4)$$

The total power consumed by the CRS is defined as:

$$P_{stage} = P_{FR} + P_{RR} = \tau_{FR} \omega_{FR} + \tau_{RR} \omega_{RR} \quad (5)$$

Finally, the static efficiency is defined as:

$$\eta_s = \frac{\Delta p_s Q_v}{P_{stage}} \quad (6)$$

3.2. Estimation of the uncertainties

The uncertainty are first estimated according to ten measurements that have been performed at the same rotation rates and for a fixed diameter of the iris damper. The final uncertainty that is given hereafter takes into account the accuracy of the measuring devices and the propagation of uncertainties.

Density of air ρ_a . According to the repetition of measurements and simple propagation of uncertainty rules, the relative uncertainty of ρ_a is $\pm 0.3\%$. Please note that all the presented results are rescaled to a reference density $\rho_a = 1.21 \text{ kg.m}^{-3}$.

Volumetric flow rate Q_v . As presented previously, the volumetric flow rate is measured by an ISO-5167 orifice plate at more than $15D$ downstream of the CRS. According to the repetition of measurements and to the accuracy of the transducers, the uncertainty of Q_v is $\pm 0.4\%$ at the design flow rate.

Correction for the losses. At the design point, the uncertainty of Δp_{drop} is about $\pm 0.9\%$, which means $\pm 1.0 \text{ Pa}$.

Static pressure rise Δp_s . The uncertainty of Δp_s is then $\pm 4 \text{ Pa}$ close to the design flow rate, that is a relative uncertainty of $\pm 1\%$ for the CRS.

Power consumption P_{stage} . The uncertainties of the total power consumption is $\pm 4.5 \text{ W}$ that is 0.8% of the power at the design point.

Static efficiency η_s . The relative uncertainty of η_s is $\pm 2\%$ (about ± 1.3 percentage points at the nominal flow rate).

3.3. Velocity measurements

The axial and tangential components of the velocity along the radial direction are measured on 25 positions from $r = 65 \text{ mm}$ to $r = 185 \text{ mm}$ using a one-component Laser Doppler anemometry LDA system through a thin and flat window, integrated to the duct. The LDA system consists of a Innova Coherent 70S continuous argon ion laser, a Dantec Dynamics Fiberflow 60mm probe system with a beam expander and a Dantec Dynamics BSA enhanced 57n20 for burst spectrum analysis. The main characteristics and dimensions of the system are given in Tab. 4. The flow is seeded with a fog generator that generates 1 to 5 μm particles. The inlet and outlet of the test-rig are enclosed in a 12 m^3 room where the fog is generated.

Laser power:	12	W
Wavelength:	488	nm
Beam diameter:	1.5	mm
Beam expander ratio:	1.85	
Focal length:	310	mm
Meas. vol. length:	590	μm
Meas. vol. thickness:	70	μm

Table 4: Characteristics of the LDA system

The LDA measurements are performed at three axial position: 5 mm upstream of the FR, half-way between the two rotors and 5 mm downstream of the rear rotor, *i.e.* at $Z_p = -46$, $Z_p = 5$ and $Z_p = 50 \text{ mm}$ (see Fig. 1 for the $Z = 0$ reference). These positions corresponds to 4% of the blade span upstream of the front rotors, downstream of the front rotors and downstream of the rear rotors, or to 10% (7.5%) of the average chord length of the front (rear) rotors.

4. Comparison of the three stages

4.1. Overall characteristics

The characteristics of the three stages and of the three front rotors working alone are shown in Fig. 2. Closed symbols stand for the front rotors working alone and open symbols stand for CRS at their nominal angular velocity ratios θ_0 . The specification point is displayed with the magenta star (\star). Two or three series of experiments performed at different days are plotted for each configuration, with variation in air density up to 3%. Once rescaled to the reference density $\rho_a = 1.21 \text{ kg.m}^{-3}$, the data fairly collapse, the discrepancy between the different series being less than 1%, *i.e.* below the estimated uncertainties. The characteristics of the rear rotors working alone are plotted in Fig. 3.

The power consumption of the different rotors working alone or in a CRS are plotted in Fig. 4. The values of the static pressure rise, static efficiency and of the power

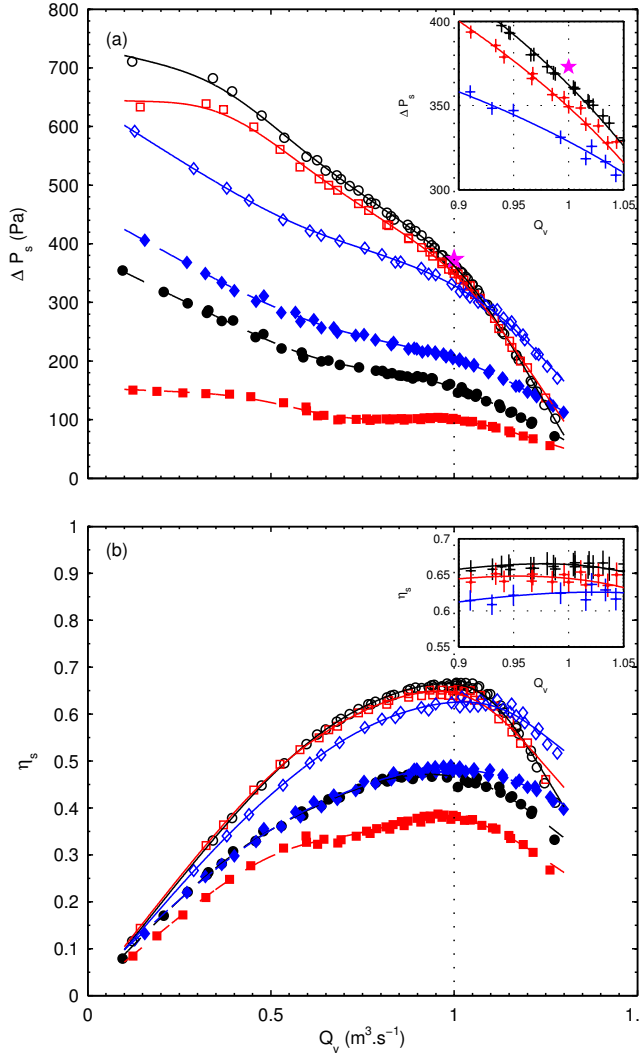


Figure 2: Overall characteristics of the counter-rotating stages (open symbols) and of the front rotors working alone (closed symbols). (a) static pressure rise Δp_s vs. volumetric flow rate Q_v , and (b) static efficiency η_s vs. volumetric flow rate Q_v . (\circ : JW1), (\square : JW2), (\diamond : JW3). (\star : specification point). The insets correspond to a zoom close to the design flow rate and the data in the insets are plotted with vertical and horizontal errorbars as discussed in § 3.2. The solid and dashed lines are smoothing splines and are used as eye guides

consumed by the front and rear rotors at the design volumetric flow rate $Q_v = 1 \text{ m}^3 \cdot \text{s}^{-1}$ are reported in Tab. 5. Finally, the ratios of the power consumed by the rear rotor to the power consumed by the whole stage for the three CRS are plotted in Fig. 5.

At first sight, the main global features that are observed are very similar to the results reported in Refs. [9, 10]. First of all, the static efficiency peak of the CRS are significantly greater than that of the front rotors working alone (see Fig. 2b). The gain in static efficiency that is observed for the CRS with respect to the FR alone is of roughly +19 percentage points for JW1, +27 for JW2, and +14 for JW3. The three CRS are thus very efficient, the typical maximum static efficiency of a traditional

	Δp_s (Pa)	η_s (%)	Power (W) (FR)	(RR)
FR1	154 ± 3	46.7 ± 1	331 ± 2.5	
JW1	362 ± 4	66.4 ± 1	335 ± 2.5	211 ± 2
FR2	99 ± 2	37.8 ± 1	263 ± 2	
JW2	349 ± 4	64.5 ± 1	271 ± 2	270 ± 2.5
FR3	204 ± 3	48.3 ± 1	422 ± 2.5	
JW3	329 ± 4	62.5 ± 1	427 ± 2.5	100 ± 1.5

Table 5: Characteristics of the three front rotors working alone and of the three counter-rotating stages at the design volumetric flow rate $Q_v = 1 \text{ m}^3 \cdot \text{s}^{-1}$

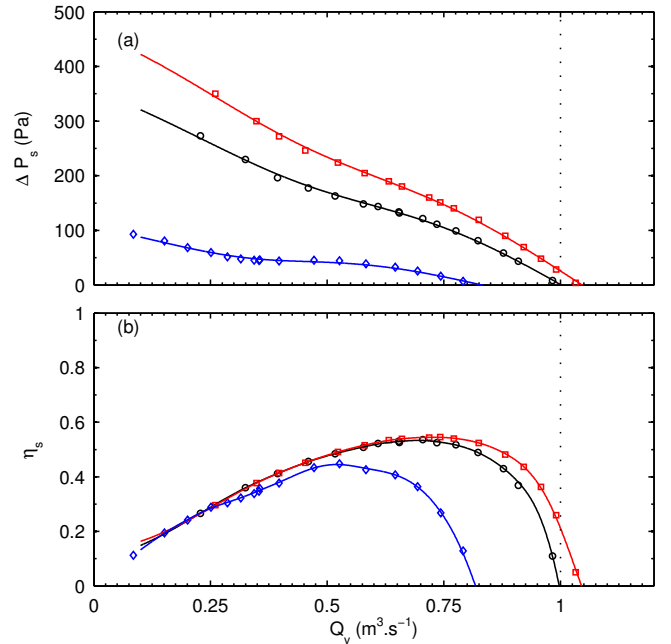


Figure 3: Overall characteristics of the rear rotors working alone. (a) static pressure rise Δp_s vs. volumetric flow rate Q_v and (b) static efficiency η_s vs. volumetric flow rate Q_v . (\circ : JW1_{RR}), (\square : JW2_{RR}), (\diamond : JW3_{RR}). The solid lines are smoothing splines and are used as eye guides

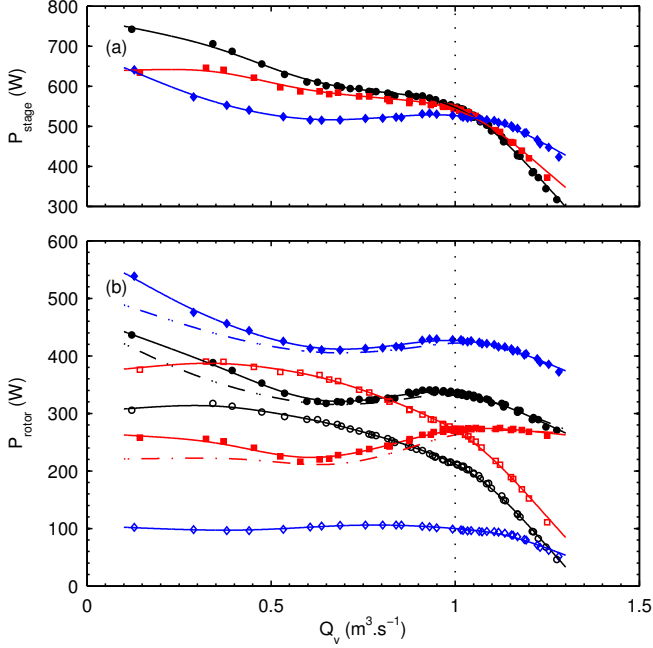


Figure 4: Power consumption of the rotors *vs.* volumetric flow rate Q_v : (a) total power consumption in the three CRS. (\bullet : JW1), (\blacksquare : JW2), (\blacklozenge : JW3). (b) power consumed by the front rotors included in a CRS (closed symbols) and by the rear rotors (open symbols). The solid lines are smoothing splines and are used as eye guides. The dash-dotted lines are smoothing splines of the data obtained for the front rotors working alone

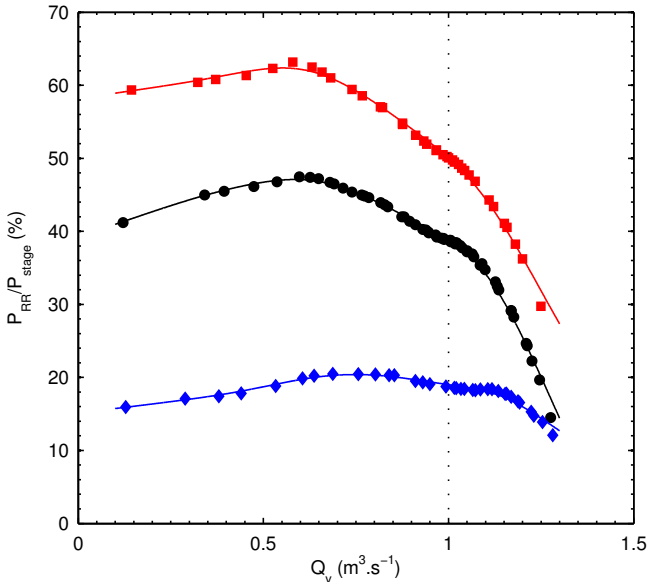


Figure 5: Ratio of the rear rotor power consumption to the CRS power consumption *vs.* volumetric flow rate Q_v . (\bullet : JW1), (\blacksquare : JW2), (\blacklozenge : JW3). The solid lines are smoothing splines and are used as eye guides

rotor-stator stage being of the order of 55% according to Ref. [22], and up to 60% for exceptional stages (see also Refs. [10, 19, 23]). Shigemitsu *et al.*[8] also reported a small increase in maximum *total* efficiency—that is based on *total* pressure rise or “head”—for a counter-rotating axial pump, with respect to a rotor-stator pump working under the same conditions.

Then, the slopes of the characteristics are steeper for the CRS than for the FR alone (see Fig. 2a), as reported also in Ref. [8]. The shapes of the static pressure rise curves of the CRS are moreover fairly well correlated to the behavior of the rear rotors, as can be seen in Fig. 3 and Fig. 4b that represents the power consumption of the rear rotors. This feature has also been reported on the two counter-rotating axial pumps studied in Ref. [2], and on the very small axial fan studied in Ref. [5].

Next, on a more quantitative point of view, the results are very satisfying. For the front rotors working alone, the measured values that are reported in Tab. 5 match within $\pm 3\%$ the predictions of the design in-house code, for the three cases. When coupling the front rotors to their rear rotors to form the three CRS that are studied here, the static pressure rise at the design flow rate is also quite well achieved for the three CRS: the third stage JW3 has a pressure rise that is 12% lower than the target, as the very first counter-rotating stage studied in Ref. [9], while the static pressure rise for JW1 is only 3% below the design value of 373 Pa.

Finally, one can observe a slight tendency for the power consumed by the FR of each CRS to increase with respect to the same isolated rotor (please compare dash-dotted lines and solid lines in Fig. 4b, and the data reported in Tab. 5). The magnitude of this increase is hardly greater than the uncertainty close to the nominal flow rate: it is of the order of 5 W. This effect is more significant at partial flow rate, where the increase is of the order of 30 to 40 W for the three CRS at volumetric flow rates lower than $Q_v \leq 0.4 \text{ m}^3 \cdot \text{s}^{-1}$. It is also more pronounced for JW2 in which the rear rotor rotates the fastest. These last two observations are consistent with the conclusions reported in Refs. [1, 2].

Looking now at the ratio of the power consumed by the rear rotor to the power consumed by the whole stage that is plotted in Fig. 5, one can notice that this ratio is very close to the design load distribution L at the design point: it is 39% for JW1, 50% for JW2 and 19% for JW3 at $Q_v = 1 \text{ m}^3 \cdot \text{s}^{-1}$ when the values of L are respectively $L = 41\%$, $L = 52\%$ and $L = 23\%$ (see also Tab. 2). One could thus infer that the *total* efficiencies of the rear and front rotors are very close. The ratio of the powers is fairly constant at partial flow rates, with a small peak value at $Q_v \simeq 0.6 \text{ m}^3 \cdot \text{s}^{-1}$ for the three CRS. On the other hand, it decreases rapidly at overhead flow rates. This is consistent with the fact that the pressure rise of the CRS rapidly decreases to a value close to the FR working alone and that the power consumed by the FR is barely affected by the RR at overhead flow rates. One would thus

expect stronger interactions or influence of the rear rotors at partial flow rates. This will be confirmed by comparing LDA measurements of the velocities in a single rotor stage (FR working alone) to a the counter-rotating stage for the three CRS (see § 4.2).

Let us now study each CRS in more details.

- JW1 (● in Figs. 2, 4 and 5). This counter-rotating stage presents the best static efficiency among the three stages, reaching $66.5 \pm 1\%$ at $Q_v = 0.97 \text{ m}^3 \cdot \text{s}^{-1}$. The front rotor working alone presents a monotonous characteristic curve. The static efficiency curve is quite flat around the design flow rate. For the counter-rotating stage, one can observe a pronounced break in the slope at $Q_v \simeq 1 \text{ m}^3 \cdot \text{s}^{-1}$. The shape of the static efficiency curve is also modified with a sharp decrease of the efficiency at small overhead flow rates.
- JW2 (■ in Figs. 2, 4 and 5). Surprisingly enough, the characteristic curves of the CRS are very close to that of JW1, although the values of θ_0 strongly differ between the two stages—the rear rotor rotating much faster in JW2—and although the front rotors JW1_{FR} and JW2_{FR} behave in a very different way. Indeed, the front rotor JW2_{FR} presents very low static efficiency and the static pressure rise curve is flat or even has a slightly positive slope. This is consistent with the low stagger angles of JW2_{FR}. At the design flow rate, the increase of the power consumption of the front rotor when coupled to the rear rotor corresponds to a 3% increase and is greater than the uncertainty of the power measurement, contrary to the JW1 case where the 1% increase is of the order of the uncertainty.
- JW3 (◆ in Figs. 2, 4 and 5) The front rotor JW3_{FR} exhibits the best performance, with a static efficiency of $48.3 \pm 1\%$ at $Q_v \simeq 0.98 \text{ m}^3 \cdot \text{s}^{-1}$. The corresponding static pressure rise curve is quite steep and almost parallel to that of JW1_{FR}. Concerning the counter-rotating stage JW3, it has a lower performance at partial flow rates than the two other CRS with a pressure rise of the order of 80 Pa lower than that of JW1 and an efficiency 8 percentage points lower than that of JW1 for $0.4 \leq Q_v \leq 0.8 \text{ m}^3 \cdot \text{s}^{-1}$. A break in the slope of the static pressure rise curve can still be observed around $Q_v \simeq 1.08 \text{ m}^3 \cdot \text{s}^{-1}$, however it is less pronounced than for JW1 and JW2. Moreover, the efficiency curve is more flat at overhead flow rates.

4.2. Averaged velocity profiles

LDA measurements of the axial and tangential components have been performed along the spanwise direction at three different flow rates. The results are plotted in Fig. 6 for $Q_v = 1 \text{ m}^3 \cdot \text{s}^{-1}$, in Fig. 7 for $Q_v = 0.6 \text{ m}^3 \cdot \text{s}^{-1}$ and Fig. 8 for $Q_v = 0.37 \text{ m}^3 \cdot \text{s}^{-1}$. The measurements that are discussed in the present Article have been performed 5 mm (4% of the blade span and 10% of the average chord

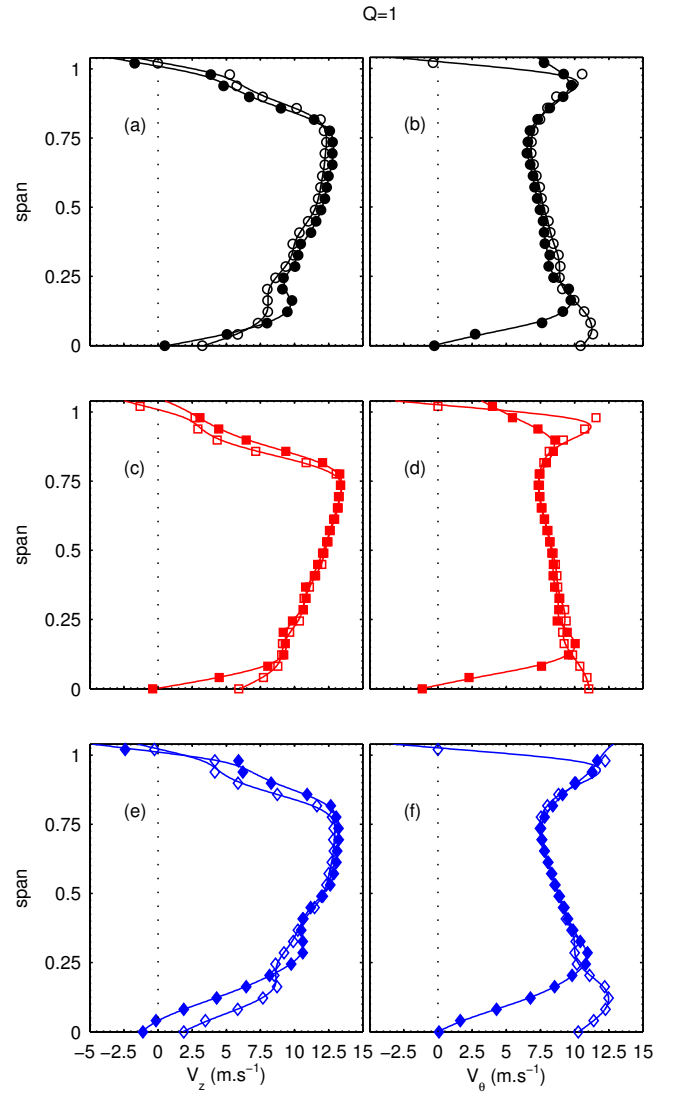


Figure 6: LDA measurements at $Z_p = 5 \text{ mm}$ downstream of the front rotor. $Q_v = 1 \text{ m}^3 \cdot \text{s}^{-1}$. (a-c-e): axial velocity V_z ; (b-d-f): tangential velocity V_θ . (a-b): ○—JW1_{FR}, ●—JW1. (c-d): □—JW2_{FR}, ■—JW2, ◆—JW3_{FR}, ◆—JW3

length) downstream of the front rotor. In each figure, the open symbols stand for the front rotors working alone, and the closed symbols stand for the counter-rotating stages. These measurement allow thus to analyse the effects of the presence of a rear rotor onto the average flow that is discharged by the front rotors, at the design flow rate, at a moderate partial flow rate and at very low flow rate.

For the design flow rate $Q_v = 1 \text{ m}^3 \cdot \text{s}^{-1}$, the overall shape of the velocity profiles are in much better agreement with the profiles predicted by the in-house code than what has been reported in Ref. [9] for the first prototype (HSN). The axial velocity profiles are indeed more flat and do not present any recirculation close to the hub for the three stages, contrary to the HSN case. This may be due to the fact that the radii of the rotor hubs have been increased from 55 mm for HSN to 65 mm for JW1, JW2 and JW3, in order to match the radius of the casing that support the motor.

For the three stages, one can notice a decrease of the axial velocity close to the hub when the rear rotor is present (closed symbols in Fig. 6a-c-e), compared to the case of a front rotor working alone (open symbols in Fig. 6a-c-e). This is compensated by a small increase of the axial velocity in the blade tip region, in order to have a constant flow rate. This characteristic is more pronounced for JW3.

In the main part of the blade span (between 20% and 90%), the rear rotors only marginally slow down the flow gyration downstream of the front rotors. However, though the average velocity profiles are hardly affected in this part of the blade, the fluctuations are twice as large —of the order of 20% of the average velocity for the counter-rotating stages, and of 10% for the front rotors alone. The tangential velocities are substantially affected by the presence of the rear rotors close to the hub and in the tip region. The strongest modifications of the average tangential velocity are observed close to the hub. This velocity is of the order of $10 \text{ m} \cdot \text{s}^{-1}$ for the front rotors working alone, while it is close to zero for the three counter-rotating stages and substantially slowed down up to 20% of the blade span. A smaller decrease of the order of 3 to $5 \text{ m} \cdot \text{s}^{-1}$ is observed in the tip region, between 90% and 97% of the blade span. This feature is strongly correlated to the rear rotor rotation rate: it is negligible for JW3 ($N_{RR3} = 1100 \text{ rpm}$), then it corresponds to a small variation for JW1 ($N_{RR1} = 2200 \text{ rpm}$) and is strong for JW2 ($N_{RR2} = 2600 \text{ rpm}$). An opposite effect is observed for the upper part of the blade tip and in the gap between the rotor and the casing (above 97% of the blade span): while the tangential velocity downstream of the front rotor rotating alone is very close to zero in this region, it is strongly increased for the counter-rotating stages.

For partial flow rates $Q_v = 0.6 \text{ m}^3 \cdot \text{s}^{-1}$ in Fig. 7 and $Q_v = 0.37 \text{ m}^3 \cdot \text{s}^{-1}$ in Fig. 8, the three systems behave differently, and the interactions between the front and rear rotors are enhanced. Concerning the case when only the front rotor is working, The JW1_{FR} (\circ) and JW3_{FR} (\diamond) give very similar velocity profiles. They both present neg-

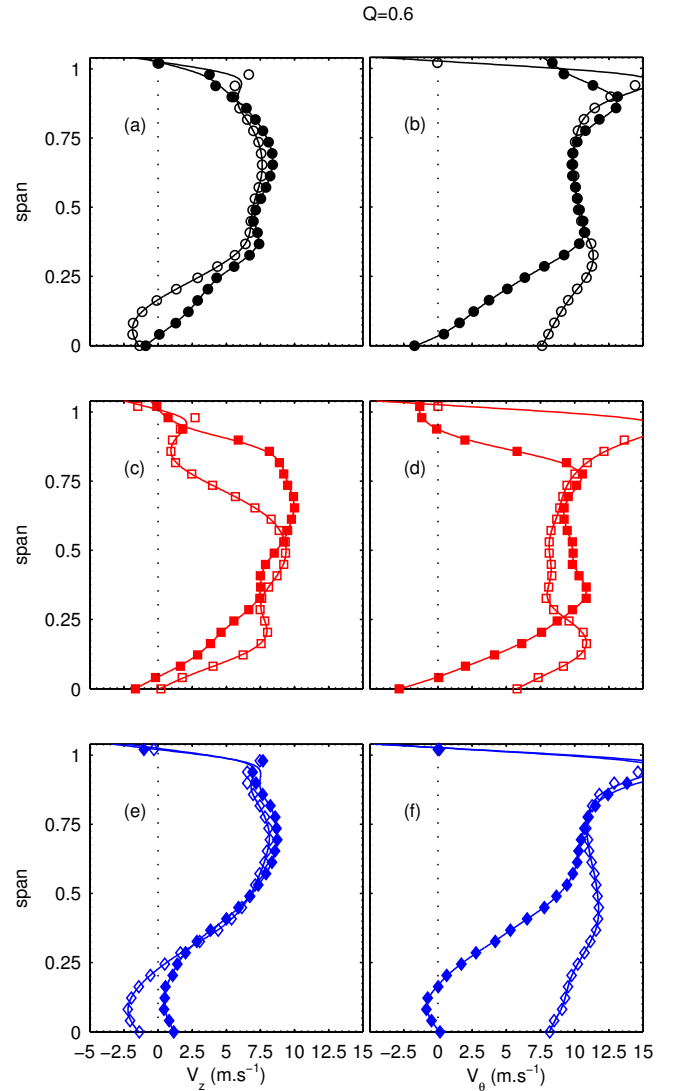


Figure 7: LDA measurements at $Z_p = 5 \text{ mm}$ downstream of the front rotor. $Q_v = 0.6 \text{ m}^3 \cdot \text{s}^{-1}$. (a-c-e): axial velocity V_z ; (b-d-e): tangential velocity V_θ . (a-b): \circ — JW1_{FR} , \bullet — JW1 . (c-d): \square — JW2_{FR} , \blacksquare — JW2 , \diamond — JW3_{FR} , \blacklozenge — JW3

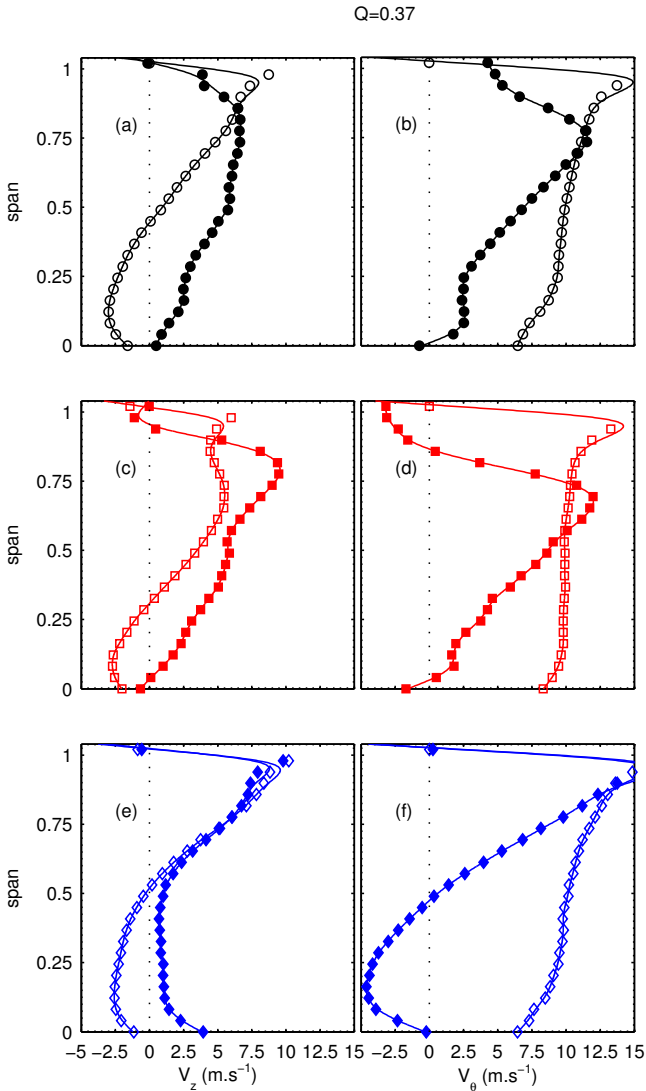


Figure 8: LDA measurements at $Z_p = 5$ mm downstream of the front rotor. $Q_v = 0.37$ m³.s⁻¹. (a-c-e): axial velocity V_z ; (b-d-f): tangential velocity V_θ . (a-b): \circ —JW1_{FR}, \bullet —JW1. (c-d): \square —JW2_{FR}, \blacksquare —JW2, \diamond —JW3, \blacklozenge —JW3

ative axial velocities, corresponding to a recirculation respectively below 17% and 22% of the blade span at $Q_v = 0.6$ m³.s⁻¹, and below 45% of the blade span for JW1_{FR}, 51% of the blade span for JW3_{FR} at $Q_v = 0.37$ m³.s⁻¹. On the contrary, the axial velocity downstream of JW2_{FR} (\square) does not present recirculation at $Q_v = 0.6$ m³.s⁻¹ and a relatively small recirculation bubble extending to 31% of the blade span at $Q_v = 0.37$ m³.s⁻¹. The same grouping —JW1_{FR} and JW3_{FR} vs. JW2_{FR}— can be made for the shape of the tangential velocity profiles. This is consistent with the fact that the shapes of the different curves —static pressure rise and static efficiency vs. volumetric flow rate in Fig. 2 and power consumed vs. volumetric flow rate in Fig. 4b— are similar for JW1_{FR} (\circ) and JW3_{FR} (\diamond), while quite different for JW2_{FR} (\square). This may be linked to the values of the stagger angle, that is large for JW1_{FR} and JW3_{FR} and significantly smaller for JW2_{FR} (see Tab. 3).

When coupling now the rear rotors to form a counter-rotating stage, one can notice large modifications at partial flow rates, for the three stages. The most salient feature is that the recirculation bubble close to the hub disappears: the axial velocity is positive all along the blade span—it is reduced in the blade tip region in that case to compensate for constant the flow rate. This could be thought as an “aspiration effect” of the rear rotor.

The slowing down of the tangential velocity that is starting at the hub extend to higher blade span as the flow rate is decreased. In the lower part of the blades, the blade span at which the axial and tangential velocity profiles for a front rotor working alone and for the counter-rotating stage get close is similar for both components for the three stages at the three flow rates: the effects of the interaction between the rotors seem to be well correlated in the lower part of the blades. This is different for the upper part of the blade and in the tip gap, where the decrease of tangential velocity seems this time to be correlated to the rotation rate of the rear rotor at the three flow rates.

4.3. Unsteady flow features

The wall pressure fluctuations are measured at a distance $Z_p = 5$ mm downstream of the front rotor, *i.e.* halfway between the two counter-rotating rotors (see Fig. 1). The microphone is a G.R.A.S 40BP 1/4” polarized pressure microphone of sensitivity 1.65 mv.Pa⁻¹, with a G.R.A.S 26AC preamplifier and a G.R.A.S 12AG power supply module. It is flush-mounted on the casing. The signals are amplified with a gain of +30 dB and high-pass filtered with a three-pole Butterworth filter with cut-off frequency of 20 Hz. The signals are then digitalized using a NI Data Acquisition Card (PCI 6123S, 16 bits) at a sample rate of 6 kHz. The power spectral density (PSD) of these fluctuations for the three systems working at three different volumetric flow rates are plotted in Fig. 9.

The different peaks that are visible in the spectra correspond to three different origins: the blade passing frequency of the front rotor (f_{FR}) and its harmonics (\blacktriangledown), the

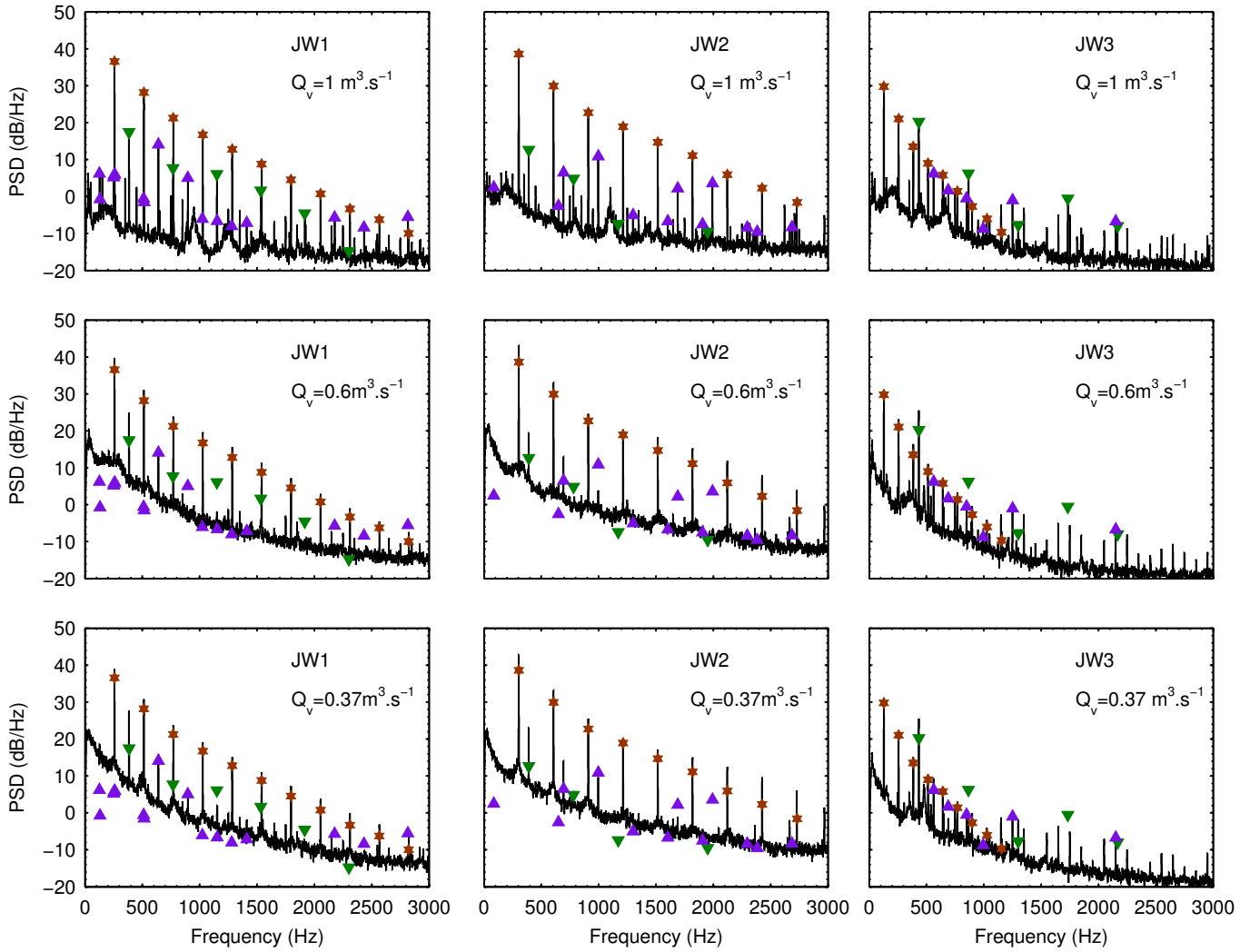


Figure 9: PSD of the wall pressure fluctuations measured at $Z_p = 5$ mm, for JW1 (left column), JW2 (middle column) and JW3 (right column). The volumetric flow rates are: $Q_v = 1 \text{ m}^3 \cdot \text{s}^{-1}$ for the first line; $Q_v = 0.6 \text{ m}^3 \cdot \text{s}^{-1}$ for the second line and $Q_v = 0.37 \text{ m}^3 \cdot \text{s}^{-1}$ for the third line. (▼): $m f_{FR}$, (★): $n f_{RR}$, and (▲): $m f_{FR} + n f_{RR}$ with $m \neq 0$ and $n \neq 0$. The symbols that are displayed in the first line are reproduced in the second and third line, in order to highlight the evolution of the amplitudes of the peaks with the flow rate

rear rotor blade passing frequency (f_{RR}) (★) and finally, the frequencies corresponding to linear combinations of the front and rear rotor blade passing frequencies (▲). Please note that, for each column —each CRS— the amplitudes of the symbols in the first line of Fig. 9 —that correspond to $Q_v = 1 \text{ m}^3 \cdot \text{s}^{-1}$ — are reported in the lines below in order to better visualize the changes in the spectra for different flow rates. The front and rear rotor blade passing frequencies are:

- $f_{FR1} = 383 \text{ Hz}$ & $f_{RR1} = 257 \text{ Hz}$;
- $f_{FR2} = 390 \text{ Hz}$ & $f_{RR2} = 303 \text{ Hz}$;
- $f_{FR3} = 433 \text{ Hz}$ & $f_{RR3} = 128 \text{ Hz}$

The amplitude of the peaks corresponding to the front rotor blade passing frequency, to the rear rotor blade passing frequency and to the dominant linear combination of these frequencies are reported in Tab. 6 for the three stages.

	f_{RR} (dB/Hz)	f_{FR} (dB/Hz)	(m,n) value (dB/Hz)	Std(p') (dB)
$Q_v = 1 \text{ m}^3 \cdot \text{s}^{-1}$				
JW1	36.5	17.4	(1,1) 14.1	40.9
JW2	38.5	12.6	(1,2) 10.9	42.9
JW3	29.8	20.2	(1,1) 6.2	35.1
$Q_v = 0.6 \text{ m}^3 \cdot \text{s}^{-1}$				
JW1	39.8	25.0	(1,1) 15.0	45.3
JW2	43.0	19.3	(1,1) 12.9	47.8
JW3	30.7	25.5	(1,1) 5.6	37.6
$Q_v = 0.37 \text{ m}^3 \cdot \text{s}^{-1}$				
JW1	39.0	27.7	(1,1) 15.8	46.0
JW2	42.7	23.0	(1,1) 14.0	47.8
JW3	28.3	25.5	(1,1) 9.3	36.7

Table 6: Amplitude of the peaks at f_{RR} , f_{FR} and $mf_{FR} + nf_{RR}$, for JW1, JW2 and JW3, at various volumetric flow rates. Std(p') represents the power of the total signal

At the design flow rate, several common features can be noticed. First, the amplitudes of the peaks corresponding to the blade passing frequency of the rear rotor and its harmonics (★) are significantly higher than that of the front rotors (▼). The influence of the rear rotor propagates upstream through a potential effect and is stronger than that of the front rotor, usually attributed to the wakes of the blades. This is the case for the three stages, though the rear rotor of JW3 rotates much more slowly than the front rotor and though the load distribution ratio of this CRS is quite low ($L = 21\%$). Then, one can notice that high rank harmonics contribute more to the pressure variance in the

case of the rear rotor than in the case of the front rotor: up to harmonic $10f_{RR1}$ vs. $5f_{FR1}$ for JW1; $9f_{RR2}$ vs. $2f_{FR2}$ for JW2 and $8f_{RR3}$ vs. $5f_{FR3}$ for JW3. Finally, there is a strong interaction between the two rotors that give rise to important peaks at various linear combinations of the two base frequencies (▲) at the design volume flow rate. If one writes the linear combination $mf_{FR} + nf_{RR}$, the dominant interaction peak corresponds to a ($m = 1, n = 1$) combination for JW1 (640 Hz) and JW3 (561 Hz) and to a ($m = 1, n = 2$) combination for JW2 (997 Hz), the ($m = 1, n = 1 - 697 \text{ Hz}$) contribution being the second peak with a value of $6.5 \text{ dB} \cdot \text{Hz}^{-1}$. The counter-rotating stage JW2 presents the highest amplitude for f_{RR} and the lowest for f_{FR} among the three CRS. This is consistent with the ratio of rotational speeds. One can moreover notice a strong correlation between the levels of peaks at the blade passing frequencies and the rotation rates of the rotors. Finally, the total level of the pressure fluctuations is obviously the lowest for JW3, and is almost similar for JW1 and JW2. This last characteristic may be correlated to the sums of the two rotation rates that are of the same order for JW1 and JW2 (4500 & 4400 rpm) and much lower for JW3 (3700 rpm).

Then, for $Q_v = 0.6 \text{ m}^3 \cdot \text{s}^{-1}$ and $Q_v = 0.37 \text{ m}^3 \cdot \text{s}^{-1}$, the overall level of pressure fluctuations are strongly increased with respect to the previous nominal flow rate. The same hierarchy between the overall level and the contribution of the first blade passing frequencies is observed. However, one can notice a remarkable change in the spectral content: the peaks corresponding to the interactions are dramatically attenuated, and in contrast, the amplitudes corresponding to both f_{FR} and f_{RR} are increased. For the CRS JW1 and JW2, the interaction peaks that barely remain are the ($m = 1, n = 1$) peaks.

5. Conclusion

Three different counter-rotating stages have been designed to meet the same pressure rise at a given flow rate. These three stages have different load distribution ratios at design point, ranging from $L = 23\%$ (low contribution of the rear rotor) to $L = 52\%$ (equal contribution of the two rotors). They also have very different angular velocity ratios, between $\theta_0 = 0.42$ and $\theta_0 = 1.44$ (the rear rotor rotates faster than the front one). The three front rotors have different characteristics, with either very flat curves or steep ones, and very low or quite high efficiency. Surprisingly enough the three CRS have similar characteristics, with a pressure rise curve that present large negative slope at all flow rates and a high static efficiency at the design flow rate. The slope of the characteristic seems correlated to the behavior of the rear rotor. The characteristic curves of JW1 and JW2 are even almost superimposed. The best stage in terms of static pressure rise and static efficiency is JW1 with a static pressure rise only 3% below the target value and an efficiency of 66.4% for a load ratio $L = 41\%$ and an angular velocity ratio $\theta_0 = 0.96$.

The same pressure rise can be achieved with the two other CRS by modifying the angular velocity of the rear rotors.

The best efficiency at $Q_v = 1 \text{ m}^3 \cdot \text{s}^{-1}$ and $\Delta p_s = 363 \text{ Pa}$ is obtained for JW2 with $N_{FR} = 1740 \text{ rpm}$ and $N_{RR} = 2695 \text{ rpm}$ ($\theta = 1.55$) that gives $\eta_s = 65.8\%$ and $L = 45\%$; it is obtained with $N_{FR} = 2455 \text{ rpm}$ and $N_{RR} = 1470 \text{ rpm}$ ($\theta = 0.6$) for JW3 leading to $\eta_s = 64.6\%$ and $L = 37\%$. The relative poor performance of JW3 could thus be greatly improved by accelerating the rear rotor by a factor 1.4. This is consistent with the velocity measurements that reveal a significant negative incidence angle for the rear rotor of JW3 under the design conditions. Another solution would have been to decrease the stagger angle of its blades.

At the design flow rate, the time-averaged flow downstream of the front rotor is barely modified by the presence of the rear rotor, with a small displacement of the discharging flow towards the blade tip, and a small slowdown of the tangential velocity close to the tip. The effect is stronger for partial flow rates: the recirculation close to the hub downstream of the front rotor is suppressed in the three CRS and this could explain the good performance at partial flow rates.

The power spectral densities of the wall pressure fluctuations between the rotors show that the dominant frequency corresponds to the blade passing frequency of the rear rotor and that the zone between the two counter-rotating rotors is a zone of high interactions between instationary flows. This feature should also be taken into account for better design and optimization. It would be very interesting to better characterize these interactions with phase-locked time-resolved measurements such as described in Refs. [12, 13]. The effect of the number of blades in each rotor may also be addressed in forthcoming experiments, with JW1 rotors of same blade cascade parameters but different blade numbers, and focusing on acoustical behaviour of the counter-rotating stages.

The design of the rear rotor is in conclusion of great importance since it triggers the working stability of the system and the level of fluctuations. For a given design point, the choice of the angular velocity ratio and of the blade loading have a direct impact on the stagger angle of the rear rotor. In our case a too few loaded rear rotor leads to a poor results (JW3) and the maximum loading of the rear rotor (JW2) gives good performances but with more noise. The best compromise is a load ratio of 40% with an angular velocity ratio of the order of 1.

References

- [1] T. Shigemitsu, T. Takano, A. Furukawa, K. Okuma, S. Watanabe, Pressure measurement on casing wall and blade rows interaction of contra-rotating axial flow pump, *Journal of Thermal Science* 14 (2005) 142–149. doi:10.1007/s11630-005-0025-z.
- [2] T. Shigemitsu, A. Furukawa, S. Watanabe, K. Okuma, J. Fukutomi, Experimental analysis of internal flow of contra-rotating axial flow pump, in: *Proceedings of the 8th International Symposium on Experimental and Computational Aerothermodynamics of Internal Flows*, 2007, pp. ISAI8-0034.
- [3] K.-S. Min, B.-J. Cha, H.-W. Seo, Study on the Contra-Rotating Propeller system design and full-scale performance prediction method, *International Journal of Naval Architecture and Ocean Engineering* 1 (2009) 29–38. doi:10.3744/JNAOE.2009.1.1.029.
- [4] S. Brizzolara, D. Grassi, E. P. Tincani, Design method for contra-rotating propellers for high-speed crafts: Revising the original lerbs theory in a modern perspective, *International Journal of Rotating Machinery* 2012 (2012) 408135. doi:10.1155/2012/408135.
- [5] T. Shigemitsu, J. Fukutomi, H. Shimizu, Influence of Blade Row Distance on Performance and Flow Condition of Contra-Rotating Small-Sized Axial Fan, *International Journal of Fluid Machinery and Systems* 5 (2012) 161–167. doi:10.5293/IJFMS.2012.5.4.161.
- [6] M. Joly, T. Verstraete, G. Paniagua, Full Design of a Highly Loaded and Compact Contra-Rotating Fan Using Multidisciplinary Evolutionary Optimization, in: *ASME Turbo Expo 2013: Turbine Technical Conference and Exposition*, 2013, pp. GT2013-94433. doi:10.1115/GT2013-94433.
- [7] C. Wang, L. Huang, Passive Noise Reduction for a Contrarotating Fan, *Journal of Turbomachinery* 137 (2014) 031007. doi:10.1115/1.4028357.
- [8] T. Shigemitsu, A. Furukawa, S. Watanabe, K. Okuma, J. Fukutomi, Internal Flow Measurement with LDV at Design Point of Contra-Rotating Axial Flow Pump, *Journal of Fluid Science and Technology* 4 (2009) 723–734. doi:10.1299/jfst.4.723.
- [9] H. Nouri, A. Danlos, F. Ravelet, F. Bakir, C. Sarraf, Experimental Study of the Instationary Flow Between Two Ducted Counter-Rotating Rotors, *ASME Journal of Engineering for Gas Turbine and Power* 135 (2013) 022601. doi:10.1115/1.4007756.
- [10] J. Wang, F. Ravelet, F. Bakir, Performance Gains Provided by the Use of a Counter-Rotating Axial-Flow Fan with Respect to a Conventional Rotor-Stator Stage, *J. Energy Power Sources* 2 (2015) 164–170.
- [11] J. Hurault, S. Kouidri, F. Bakir, Experimental investigations on the wall pressure measurement on the blade of axial flow fans, *Experimental Thermal and Fluid Science* 40 (2012) 29–37. doi:10.1016/j.expthermflusci.2012.01.018.
- [12] J. M. Fernández Oro, K. M. Argüelles Díaz, C. Santolaria Morros, E. Blanco Marigorta, On the structure of turbulence in a low-speed axial fan with inlet guide vanes, *Experimental Thermal and Fluid Science* 32 (2007) 316–331. doi:10.1016/j.expthermflusci.2007.04.008.
- [13] J. M. Fernández Oro, K. M. Argüelles Díaz, M. Rodríguez Lastra, M. Galdo Vega, B. Pereiras García, Converged statistics for time-resolved measurements in low-speed axial fans using high-frequency response probes, *Experimental Thermal and Fluid Science* 54 (2014) 71–84. doi:10.1016/j.expthermflusci.2014.02.002.
- [14] L.-S. Cho, H. Choi, S. Lee, J.-S. Cho, Numerical and Experimental Analyses for the Aerodynamic Design of High Performance Counter-Rotating Axial Flow Fans, in: *ASME 2009 Fluids Engineering Division Summer Meeting*, 2009, pp. FEDSM2009-78507. doi:10.1115/FEDSM2009-78507.
- [15] L. Cao, S. Watanabe, S. Momosaki, T. Imanishi, A. Furukawa, Low Speed Design of Rear Rotor in Contra-Rotating Axial Flow Pump, *International Journal of Fluid Machinery and Systems* 6 (2013) 105–112. doi:10.5293/IJFMS.2013.6.2.105.
- [16] J. Wang, F. Ravelet, F. Bakir, Influence of Design Parameters on the Global Performances of Low-Speed Counter-Rotating Axial-Flow Fans, in: *ASME 2014 4th Joint US-European Fluids Engineering Division Summer Meeting*, 2014, pp. FEDSM2014-22172. doi:10.1115/FEDSM2014-22172.
- [17] R. Noguera, R. Rey, F. Massouh, F. Bakir, S. Kouidri, Design and analysis of axial pumps, in: *ASME Fluids Engineering, Second Pumping Machinery Symposium*, Washington, USA, 1993, pp. 95–111.
see also: R. Rey, R. Noguera, F. Bakir, Pompes rotodynamiques- Aérodynamique des profils et aubages de pompes hélices, *Techniques de l'ingénieur TIB173DUO*

- (2013) bm4304. doi:<https://www.techniques-ingenieur.fr/base-documentaire/mecanique-th7/machines-hydrauliques-pompes-et-helices-42173210/pompes-rotodynamiques-bm4304/>.
- [18] J. Vad, Forward Blade Sweep Applied to Low-Speed Axial Fan Rotors of Controlled Vortex Design: An Overview, *ASME Journal of Engineering for Gas Turbine and Power* 135 (2012) 012601. doi:10.1115/1.4007428.
- [19] C. Sarraf, H. Nouri, F. Ravelet, F. Bakir, Experimental study of blade thickness effects on the overall and local performances of a Controlled Vortex Designed axial-flow fan, *Experimental Thermal and Fluid Science* 35 (2011) 684–693. doi:10.1016/j.expthermflusci.2011.01.002.
- [20] L. Herrig, C. Emery, R. Erwin, Systematic two dimensional cascade tests of naca65-series compressor blades at low speeds, Tech. Rep. Tech. Rep. TN3916, National Advisory Committee for Aeronautics (1957).
- [21] S. L. Dixon, C. A. Hall, *Fluid Mechanics and Thermodynamics of Turbomachinery*, 6th Edition, Elsevier Inc., 2010.
- [22] F. Bakir, S. Moreau, Efficient stator design for automotive engine cooling fan systems, in: *ASME 2002 Joint U.S.-European Fluids Engineering Division Conference*, 2002, pp. FEDSM2002-31318. doi:10.1115/FEDSM2002-31318.
- [23] S. C. Yen, F. K. T. Lin, Exit Flow Field and Performance of Axial Flow Fans, *ASME Journal of Fluids Engineering* 128 (2006) 332–340. doi:10.1115/1.2169809.